CHAPTER 3

High purity Fe_3S_4 greigite microcrystals for magnetic and electro-chemical performance[2]

In this chapter, we investigated the fundamental properties of a rarely reported iron sulfide: greigite (Fe_3S_4). High purity Fe_3S_4 is first synthesized by a simple hydrothermal method. The as-prepared material has the largest saturation magnetization than of all reported values and showed no low temperature transition between 5K- 300K. Raman spectra of greigite were measured both in air and vacuum, and were in good agreement with theoretical calculations. The application of the synthesized crystals as anode materials of lithium ion batteries is also investigated. The results showed excellent initial capacity and possible reactions occurring at the electrode are also discussed here.

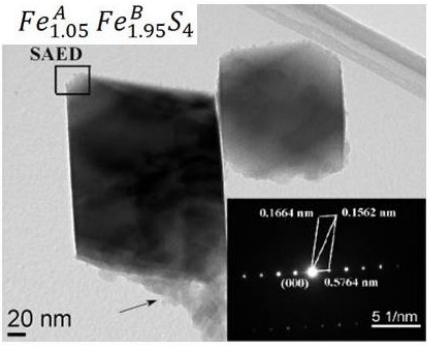

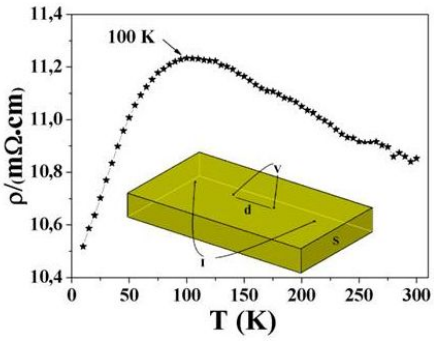

[2] This chapter is based on G. Li, B. Zhang, F. Yu, A. A Novakova, M. S Krivenkov, T. Y Kiseleva, L. Chang, J. Rao, A. O Polyakov, G. R Blake, R. de Groot, T. T. M. Palstra, High-Purity Fe_3S_4 greigite microcrystals for magnetic and electrochemical performance, Chem. Mater., 2014, 26 (20), 5821–5829.

3.1 Introduction

Greigite (Fe_3S_4) was discovered in silt and clay sediments in 1964 in California.[1] Its formation accompanies the decomposition of organic matter in the biogeochemical and bacterial sulphate reduction process.[2] However, greigite was initially believed to be palaeomagnetically unimportant due to its thermodynamic metastability and lack of any lasting record on geological time scales.[3] This traditional viewpoint changed when greigite was discovered in the sediments of Loch Lomond, indicating greater thermodynamic stability than previously proposed.[4, 5] Interestingly, greigite provides clues in the search for life on Mars. In the martian meteorite ALH84001, which is proposed to have crystallized from molten rock 4 billion years ago, an elongated multicrystalline core of greigite was found inside an organic envelope.[6, 7] This may be from the fossil remains of martian biota.

Greigite is also of interest in modern material science. Recent band structure calculations revealed that Fe_3S_4 shows a complex Fermi surface with a unique influence of relativistic effects: two sheets of the Fermi surface (dis)appear depending on the direction of an applied magnetization. This enables spintronics on the level of a single compound, rather than using traditional heterostructure devices.[8] Fe_3S_4 is also a potential anode material in lithium-ion batteries (LIBs). The use of Fe_3O_4 in LIBs has been researched extensively because of its high theoretical capacity.[9] As discussed later, Fe_3S_4 has a theoretical capacity of 785 mAh/g, two times higher than the conventional anode material graphite (372 mAh/g). Considering that greigite is nontoxic and abundant, it is an ideal material for high performance LIBs. Furthermore, greigite also has potential applications in hydrogen storage, cancer hyperthermia, and magnetic guided delivery of drug. [10-12]

Greigite is an iron thiospinel and has the same inverse spinel structure as its oxide counterpart magnetite, Fe_3O_4. The crystallographic structure of Fe_3S_4 is displayed in Figure 1. The unit cell consists of eight Fe_3S_4 moieties (space group: *Fd*-3*m*). The S atoms form a face-centered-cubic lattice, in which 1/8 of the tetrahedral *A*-sites are occupied by Fe^{3+} and 1/2 of the octahedral *B*-sites are equally occupied by Fe^{2+} and Fe^{3+}. A neutron powder diffraction study indicated a collinear ferromagnetic structure in which the iron moments on the tetrahedral and octahedral sites are antiparallel.[13] No spin canting or significant cation vacancy concentration was observed for either sublattice.[14] It is generally accepted that the magnetic easy axis of greigite is [100] at all temperatures, rather than the [111] direction of magnetite. However, there is no exact experimental confirmation.[15]

Despite the studies referred to above, greigite has received much less attention than well-studied Fe_3O_4 due to its metastable nature. It has been demonstrated that Fe_3S_4 is converted to a mixture of pyrrhotite ($Fe_{1-x}S$) and either pyrite (FeS_2) or sulfur when heated in air between 180 to 200 °C, and finally to Fe_3O_4 and maghemite (γ-Fe_2O_3). Although it is relatively stable in argon gas, Fe_3S_4 still decomposes above 250 °C.[16] The absence of pure samples of either natural or synthetic greigite has thus far hindered precise determinations of its physical and chemical properties, including saturation magnetization, Curie temperature T_c, the first anisotropy constant K_1, and the electrical conductivity. Several synthesis methods have recently been reported. Akhtar et al.[17] prepared precursor dithiocarbamato Fe^{3+} complexes and then performed thermolysis in oleylamine at different temperatures. Greigite was always the dominant product but often coexisted with a lower concentration of FeS. Zhang et al.[18] prepared relatively pure Fe_3S_4

nanoparticles by heating a $Fe(Ddtc)_3$ (Ddtc = diethyldithiocarbamate) precursor in an oleic acid / oleylamine / 1-octadecene solvent. Hydrothermal methods, which are carried out at high pressure (>2MPa) and low temperature (<300 °C) have been widely used in the synthesis of nanoarchitectured materials.[19, 20] For example, a hydrothermal method in an external magnetic field allowed either greigite or marcasite (FeS_2) to be selectively synthesized in the form of microrods.[21] Using a similar method, Chang et al.[22] synthesized polycrystalline greigite. It is difficult to obtain pure synthetic greigite because most procedures simultaneously produce other iron sulfides such as mackinawite (FeS) and pyrite (FeS_2). This is often apparent in previous reports from poor quality X-ray diffraction patterns that contain impurity peaks and broad greigite peaks that imply poor crystallinity. Low values of the saturation magnetization, M_s, also imply poor quality samples, with in most cases $M_s < 2.5\ \mu_B$ /fu compared to the expected $4\ \mu_B$ /fu (see summary in Ref. 24).[23-25]

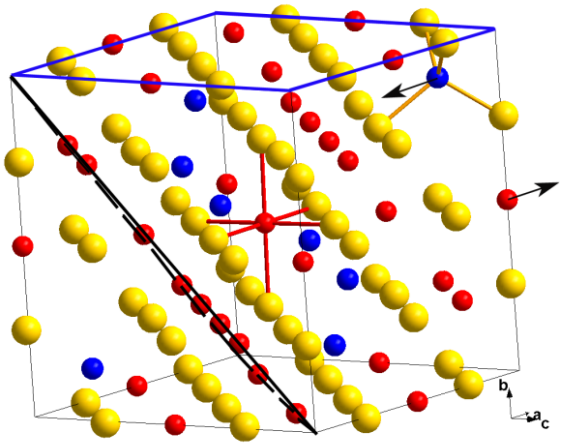

Figure 3.1 Crystal structure of Fe_3S_4 with the (001) and (111) planes outlined in blue and black, respectively. Sulfur atoms (yellow spheres) form a cubic close-packed lattice: 1/8 of the tetrahedral A sites are occupied by Fe^{3+} (blue spheres) and ½ of the octahedral B sites are occupied by Fe^{2+} and Fe^{3+} (red spheres) equally. The magnetic moments on the A and B sites are antiparallel and aligned along the [100] crystallographic axis (indicated by arrows).

Herein, a simple hydrothermal method is developed to synthesize high purity greigite. By carefully controlling the reaction temperature, reaction time, and the quantity of surfactant, greigite microcrystals with a (truncated) octahedral shape and size ~1 μm can be synthesized. The as-prepared product has a larger saturation magnetization and lower resistivity than all previous reports. The performance of high purity greigite as an anode material in LIBs is also studied. A high capacity is maintained up to 100 cycles, making it an excellent prospective electrode material.

3.2 Method

3.2.1 Synthesis

Nitrogen gas was bubbled for at least 30 minutes through 35 mL of H_2O to remove all dissolved oxygen before the synthesis. In a typical experiment, (0.6 mmol, 0.2187 g) of the surfactant cetrimonium bromide (CTAB) was dissolved in the water under continuous stirring to form a solution. After 10 minutes, (3 mmol, 0.365 g) of L-cysteine and (2 mmol, 0.2535 g) of FeCl2 were added to the solution. The solution was stirred for another 10 minutes, and then transferred into a 50 mL Teflon-sealed autoclave. The autoclave was kept at 165 °C for 40 h before being cooled to room temperature in air. A black precipitate was collected and washed with distilled water and ethanol three times. Finally, the product was heated at 60 °C under vacuum for 8 h.

3.2.2 Characterization

Room temperature power X-ray diffraction (XRD) data were recorded with a Bruker D8 Advance diffractometer equipped with a Cu Kα source (λ= 0.15406 nm). XRD data at 20 K were collected using a Huber G670 diffractometer operating with Cu Kα radiation and equipped with a closed-cycle refrigerator. The morphology and crystal structure were examined using a Philips XL 30 scanning electron microscope (SEM) and a JEM 2010F transmission electron microscope (TEM) operated at an accelerating voltage of 200 KV. The magnetization was measured using a Quantum Design MPMS-XL7 SQUID magnetometer. Mössbauer spectra were measured at room and liquid nitrogen temperatures using a constant acceleration spectrometer MS-1104M with a ^{57}Co(Rh) radiation source. For measurement of the electronic properties, a rectangular shaped polycrystalline sample was prepared by pressing Fe_3S_4 particles under 3×10^7 Pa pressure for 15 min. The electrical contacts were made using Pt wire (0.05 mm in diameter) connected to the sample by silver paint. The measurements were performed using a commercial Quantum Design Physical Properties Measurement System (PPMS) and an Agilent 3458a multimeter. Raman spectra were measured in a backscattering configuration using a liquid nitrogen cooled charged coupled device (CCD) connected to a three grating micro-Raman spectrometer (T6400 Jobin Yvon). The incident laser power was limited to 0.5 mW to avoid oxidation of the sample using excitation wavelengths of 632.8 nm.

Details of phonon calculations related to the Raman spectroscopy are described in the Supporting Information.

3.2.3 Electrochemical measurements

To fabricate the anode of a coin cell battery, the as-obtained Fe_3S_4 powder was mixed with acetylene black and polyvinylidene fluoride (PVDF) in a weight ratio of 80:10:10 in N-methyl-2 pyrrolidinone (NMP). The obtained slurry was coated onto copper foil, dried at 120 °C for 12h, and then punched into round plates of diameter 12.0 mm to form anode electrodes. Finally, the prepared anode, a Celgard2400 separator (diameter 16.0mm), a lithium cathode, and an electrolyte consisting of 1M LiPF6 in ethylene carbonate (EC) / diethyl carbonate (DEC) / ethyl methyl carbonate (EMC) (1:1:1 vol.%) were assembled into a coin cell (CR2032) in an argon filled glove box (H2O and O2<1ppm). The coin cells prepared were kept at room temperature for ten minutes at 4.2V during charging and examined using a Maccor Series 4200 standard battery test system at various

charge/discharge rates between 0.01-3V. Cyclic voltammetry (CV) was collected using an Autolab PGSTAT30 electrochemical workstation.

3.3 Results and discussion

3.3.1 Phase and morphology characterization

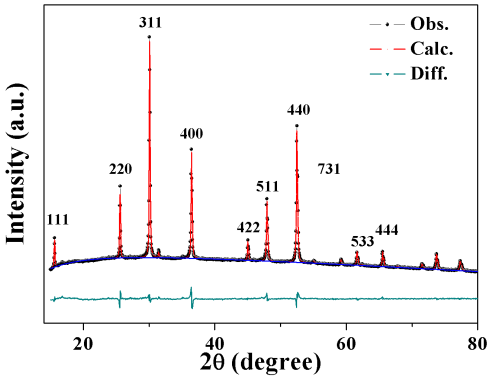

Fig. 3.2 Observed (black data points), calculated (red line) and difference (light blue line) XRD patterns of the as-prepared sample at room temperature.

Observed, calculated and difference powder XRD profiles of the obtained product at room temperature are presented in Fig. 3.2. All the peaks can be indexed in the cubic Fe_3S_4 spinel structure with space group Fd-3m (PDF card No. 16-0713). No peaks belonging to sulfur or to other iron sulfides or oxides were observed, implying that no crystalline impurities were present at more than 1% by weight. The refined lattice parameter was a = 9.8719 (1) Å, which is in good agreement with the reported value for greigite.[26] The refined atomic coordinate of sulfur on the 32e site was x = y = z = 0.2546(1), in perfect agreement with calculations.[8] Other than a contraction of the unit cell, the refined structure at 20 K was essentially the same as at room temperature; details are given in the Supporting Information Figure S1. The molar ratio of Fe to S was 2.99:4 according to energy-dispersive X-ray spectroscopy (EDS) analysis (Figure S2), consistent with a stoichiometric Fe_3S_4 sample. It should be noted here that the synthesis of pure, stoichiometric greigite requires carefully optimized experimental parameters. A small difference in the reaction temperature, the quantity of CTAB, and the purity of the starting materials (in particular $FeCl_2$) will lead to the formation of second phases such as S or Fe_2O_3.

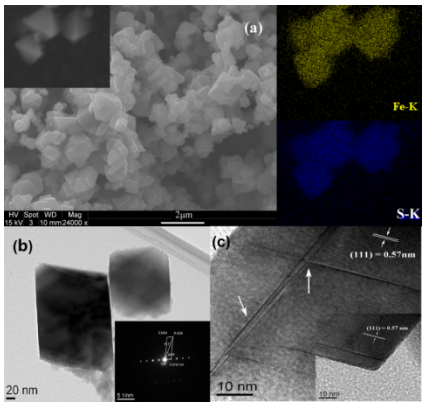

Figure 3.3 (a) SEM image of Fe_3S_4 crystals synthesized in this work: three typical octahedra are presented in the upper left inset, and the corresponding elemental maps are shown in the right-hand panel (yellow for Fe, and blue for S). (b) TEM image of two Fe_3S_4 crystals and corresponding SAED pattern (inset). (c) HRTEM lattice image of the edge and corner (inset) of a typical crystal.

The morphology of the sample was characterized by SEM and TEM, as shown in Figure 3. The SEM images in Figure 3.3a reveal that the product consists of well dispersed microcrystals with uniform (truncated) octahedral shapes. These (truncated) octahedra are fully developed and composed of eight [27] planes with a mean edge length of ~1 µm. Elemental mapping of the crystals indicates that the S and Fe are distributed homogeneously. It has been demonstrated that greigite is very sensitive to oxygen and can be oxidized to iron oxide, especially in wet conditions.[16] However, we did not detect oxygen on the surface of the crystals, which implies that high purity greigite is more stable than expected. In accordance with the SEM results, TEM images (Fig. 3.3b) show the morphology of the crystals in more detail. The selected area electron diffraction (SAED) pattern recorded along the [1 -3 4] zone axis direction can be uniquely indexed. Although some stacking faults can be identified in the high-resolution TEM (HRTEM) image in Fig. 3.3c (indicated by arrows), the clear lattice fringes confirm that the entire octahedron is a single crystal. The spacing of the fringes is 0.57 nm, which corresponds well to the (111) interplanar distance in greigite.

3.3.2 Mössbauer spectra

Fig. 3.4a shows the room temperature (RT) ^{57}Fe Mössbauer spectrum of our sample. The corresponding spectrum at 80 K is shown in Figure S3. Both spectra were best fitted with three sextets corresponding to one tetrahedral (A site) and two magnetically non-equivalent octahedral (B sites). The hyperfine interaction parameters extracted from the fits are listed in Table S1. We did not detect signals belonging to any paramagnetic phase (FeS_2) or oxidation product (Fe_3O_4 or Fe_2O_3), in contrast to previous studies.[28] The isomer-shifts for the A site are 0.27 and 0.37 mm/s at RT and 80 K (Fig S3), respectively, which are attributed to the high spin Fe^{3+} state.[29] The hyperfine field of the A site is 3.14 T at RT, and increases slightly to 3.19 T at 80 K. The fit unambiguously indicates that only Fe^{3+} occupies the tetrahedral site in this temperature range. This implies that greigite has a fully inverse spinel structure. As shown in Table S1, the isomer shifts of the B_a and B_b sextets are 0.53

and 0.54 mm/s at RT, and 0.67 and 0.65 mm/s at 80 K. (B_a and B_b represent the two non-equivalent *B* sites, the detailed meaning of which is explained below.) Thus, both sites have the same isomer shift within experimental error. However, the hyperfine field of the Ba site is always larger than that of the B_b site (3.14 T versus 3.05 T at RT, and 3.29 T versus 3.19 T at 80 K). The same result was recently obtained in a study of greigite nanoparticles of different sizes, but here the third sextet was attributed to the hexagonal smythite phase.[30] Smythite was first assigned the same chemical formula as greigite, Fe_3S_4,[31] but this was subsequently revised to Fe_9S_{11}.[32] The difference in symmetry between smythite and greigite means that they can easily be distinguished by XRD. Considering the high purity of our sample, it is reasonable to assume that the third sextet is intrinsic to greigite.

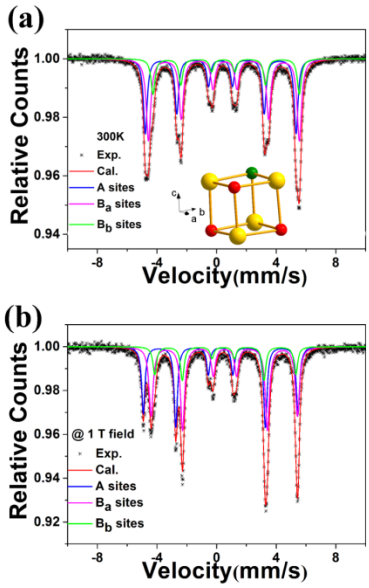

Fig. 3.4 (a) Room temperature ^{57}Fe-Mössbauer spectrum of the Fe_3S_4 microcrystals in zero field. One octant of the cubic unit cell of greigite is shown (inset), where the yellow spheres are sulfur and the red and green spheres denote two non-equivalent octahedral site iron cations. (b) ^{57}Fe-Mössbauer spectrum in a magnetic field of 1 T.

The value of the isomer shift shows that valence state of the *B*-site iron ions is between 2+ and 3+, as it is for magnetite due to fast electron hopping. We also note that H_{hyp} for the *A* site increased with applied external magnetic field, whereas H_{hyp} for the B_a and B_b sites decreased by nearly the same values (see Figure 4B and Table S1). Both observations – the same isomer shifts and the same reaction to the external magnetic field, confirm that the third component of the spectra corresponds to the B-site iron ions. The nature of two non-equivalent B-site positions for magnetite is discussed in Ref. 29 and we tend to the same explanation for greigite.

For a dominating magnetic hyperfine interaction, the Mössbauer resonance lines are shifted according to first-order perturbation theory by an amount proportional to

$(3\cos^2\theta - 1)$, where θ is the angle between the local hyperfine field H_{hyp} and the local symmetry axis (the [111] axes for the B-site).[33] If we assume that the direction of the easy magnetization for greigite is [001] as generally accepted, then the angle between the main axis of the EFG (electric field gradient tensor) and H_{hyp} would be the same for all four Fe ions. This implies that only one sextet would be observed for the B site, which contradicts our experimental data. If instead the easy magnetization direction is along [111] as in magnetite, then θ = 90° for ¾ of the B-site cations (red spheres in Figure 4a) and θ = 0 for the remaining ¼ of the B-site cations (green sphere in Figure 4a). This will yield two B-site subspectra with relative intensities of 3 : 1. For our data the ratio is 2.6 : 1 at 300 K but only 1.8 : 1 at 80 K. Two B-site sextets with an intensity ratio of 3 : 1 have also been observed in Mössbauer spectra of Fe_3O_4 above the Verwey transition.[33-35] Furthermore, ferromagnetic resonance (FMR) spectroscopy on greigite indicates a negative magnetocrystalline anisotropy constant $K1$, the same as in magnetite.[36] In a cubic crystal, the lowest order terms in the magnetocrystalline anisotropy energy can be written as

$$E/V = K_1 (\alpha^2\beta^2 + \beta^2\gamma^2 + \alpha^2\gamma^2) + K_2 \alpha^2\beta^2\gamma^2,$$

where α, β and γ are the direction cosines of the magnetization. Thus, the easy axis is determined by both K_1 and K_2 if K_2 is not assumed to be zero. The work of Winklhofer et al. indicates a similar value of K_2/K_1 of + 0.30 to 0.33 for different anisotropy models.[37] This clearly indicates an easy axis in the [111] direction. Thus, we can conclude that greigite has an easy magnetization axis along the [111] direction, rather than the [100] direction reported in previous work. We conclude that the direction of H_{hyp} with respect to the easy axis is the most likely explanation for the two B-site sextets in greigite. The significant difference from the theoretical intensity ratio of 3 : 1 at 80 K might indicate that the easy axis moves away from [111] at low temperature; for example, a 1 : 1 ratio would be expected for an easy axis of [110].[33] The application of an external magnetic field aligns the spins in one direction. Indeed, this ratio increased to 2.8 : 1 when a magnetic field of 1 T parallel to the γ beam was applied at 300 K (Fig. 3.4b and Table S1).

We note that H_{hyp} for the A site increased by 8 kOe with applied field, whereas H_{hyp} for the B_a and B_b sites decreased by 9 kOe and 11 kOe, respectively. This also proves that the Fe ions on the A and B sublattices are antiferromagnetically coupled via superexchange.

3.3.3 Magnetic property

Magnetic hysteresis loops at 5 K and 300 K of our greigite sample are presented in Fig. 3.5a and Figure S4, respectively. Typical ferrimagnetic behavior is observed in the measured temperature range, with a coercive field H_c = 92 Oe and a remanent magnetization Mr = 0.4 μ_B/f.u. at 5 K. Considering that Fe_3S_4 is a soft magnetic material according to the hysteresis loops and that the crystal dimension is in the micrometer scale, we can approximate the saturation magnetization with:

$$M = M_s (1 - aH^{-1} - bH^{-2}) + cH^{1/2},$$

where M is the magnetization, M_s is the saturation magnetization, a, b, and c are constants that describe the structural inhomogeneity within the sample, the magnetic anisotropy energy and the paraeffect caused by the external field, respectively.[38] The fitting of the magnetization curves in the first quadrant for the applied field $H > H_c$ is displayed in Fig. 3.5a, which shows excellent agreement with the experimental data. The

magnetization curve is determined by microstructural inhomogeneities in the low external field range. By plotting the M versus H^{-1}, a linear relationship is obtained below 1.2 T, as shown in Fig. 3.5b. The slope of 0.1146 Oe indicates that these microstructural inhomogeneities act as stress centers in the spin alignment around them. The deviation of the linear relationship at high field can be attributed to the paraprocess. This can be seen in the variation of M_s as function of $H^{1/2}$ (Fig. 3.5b) for fields > 3.2 T. Unfortunately, we cannot compare the level of inhomogeneity and the paraprocess in Fe_3S_4 with previous data in the literature. Nevertheless, we can establish precise values of M_s of 3.74 μ_B (70.56 emu/g) at 5 K and 3.51 μ_B (67.16 emu/g) at RT. These values are significantly larger than in previous reports of greigite (the highest reported value was M_s = 3.4 μ_B at 5 K [13]). The high M_s allows easy separation of the greigite crystals from the solution when a magnet is placed near the glass bottle (see inset to Fig. 3.5a). Coey et al. predicted assuming a purely ionic model that M_s should be 4 μ_B.[34] The magnetization measured in our current work approaches this value and is an indicator of the high quality of the sample. However, it is important to address the difference between our experimental and expected values. It is probable that the moment is lowered from 4 μ_B due to covalency: our recent band structure calculations predicted a magnetization of 3.38 μ_B in greigite.[8] Similar results have also been reported by other groups.[23, 24] First principle calculations based on the GGA + U model with U_{eff} = 1.16 eV give sub-lattice magnetizations of m_A = 3.05 μ_B and m_B = 3.25 μ_B, both of which are significantly decreased compared with the purely ionic model. Generally, the increase in covalency is caused by the overlap of wave functions between Fe and S ions, which from the band point of view corresponds to a higher degree of hybridization between the sulfur 3p and iron 3d bands. Thus, the ordered moment is lowered. The increased covalency effect is also suggested by the lower hyperfine fields in greigite than magnetite,[39] with values in the range 30.5-31.4 kOe in greigite and 45.8-49.2 kOe in magnetite.[29]

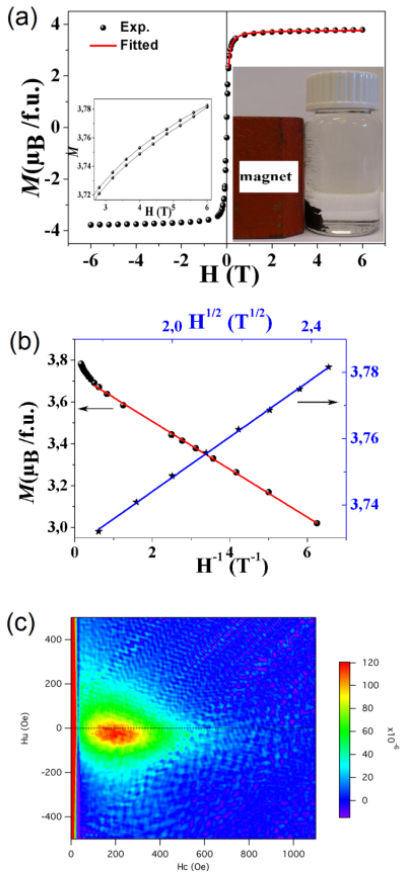

Fig. 3.5 (a) Magnetization versus field loop measured at 5 K. The inset shows the magnetic separation of Fe_3S_4 crystals from aqueous solution using an external magnet. (b) Magnetization versus H^{-1} (black) and $H^{1/2}$ (blue) for the loops at 5 K. (c) FORC diagram of the crystals.

Another contribution to the reduction of the saturation magnetization could be caused by surface spins. Previous research identified the existence of a core of aligned spins surrounded by a shell with moments inclined to the direction of the net magnetization in both $CoFe_2O_4$ and $NiFe_2O_4$ inverse spinel nanocrystals with single magnetic domains. We note that a small proportion of particles in our sample have sizes smaller than 10 nm (as indicated by the black arrow in Fig. 3.3b and Figure S5). A lowered magnetic moment was also observed in $NiFe_2O_4$ coated with an organic surfactant (oleic acid) due to surface spin canting.[40-42] If we magnify our magnetization loops at 5 K, it is clearly visible that the loop is open (inset to Fig. 3.5a) for both positive and negative field sweeps up to 6 T. This opening indicates that some of the magnetic spins have a "switching field" larger than 6 T. A similar phenomenon was also observed in milled $NiFe_2O_4$ spinel.[43] We recorded first-order reversal curve (FORC) diagrams,[44] which are able to probe domain states and the extent of magnetostatic interactions (Fig. 3.5c). The as-prepared samples have FORC

distributions with concentric inner contours with high coercivity and strong magnetostatic interactions. This is characteristic for pseudo single-domain (PSD) greigite.[45] It is well known that the spins are completely aligned by exchange interactions in sufficiently small PSD crystals, and that the rotation barriers induced by magnetocrystalline and magnetoelastic anisotropy can trap particles in two or more metastable orientations.[43] We should thus carefully consider the role of CTAB in the synthesis. It has been shown in previous work that CTAB can bond to metal cations via the polar end of the molecule. In our case, the $(C_{19}H_{42})N^+$ group in CTAB will interact with the Fe^{2+} or Fe^{3+} on the (111) faces of the growing crystals (Fig. 3.3). The surface energy of these faces is thus decreased and finally preserved after the hydrothermal reaction.[46] This results in octahedral crystals with eight [27] faces as shown in the SEM images. The influence of the surfactant is still present in the final product, because complete removal of the surfactant from the crystals is difficult.[47] The CTAB groups will interact with the Fe^{2+} or Fe^{3+} at the surface, and thus result in a surface spin canting and a lower M_s.[47] The reduction in M_s is 4.2% in our sample, much smaller than the reduction of nearly 20% in nanocrystalline $NiFe_2O_4$ but comparable with that in surfactant-coated Fe_3O_4.[42]

3.3.4 Raman spectra of greigite

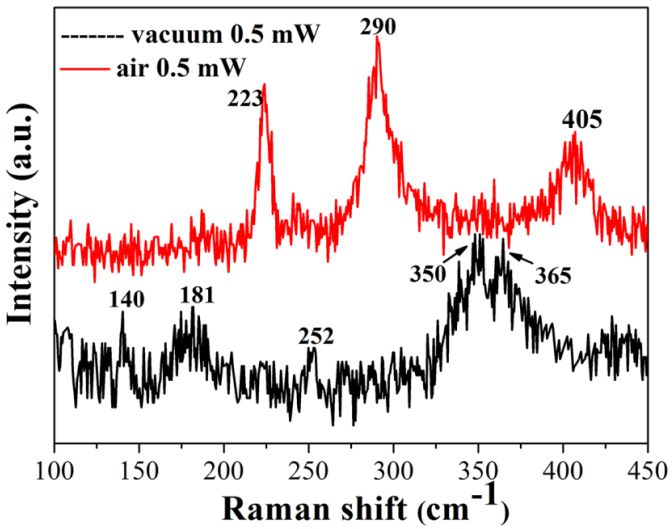

Fig. 3.6 Room temperature Raman spectra of Fe_3S_4 measured in vacuum (black) and air (red).

The lattice dynamics of greigite has been little studied; there is currently only one report on Raman spectroscopy of greigite at room temperature.[48] This sample was contaminated by mackinawite (FeS) and precise information on the positions of the greigite Raman peaks is still lacking. A group theory analysis on inverse-spinel greigite (space group Fd-3m with a reduced unit cell (Fe_6S_8) that contains 14 atoms) predicts five Raman active modes: A_{1g}, E_g, and three T_{2g}.[49]

	A_{1g}	E_g	$T_{2g\,1}$	$T_{2g\,2}$	$T_{2g\,3}$
Exp.	365	181	350	252	140
Cal.	327	180	312	238	142
Ions involved	S	S	S, Fe_{tera}	S, Fe_{tetra}	S, Fe_{tetra}

Table 3.1 Measured and calculated zone center phonon frequencies

The measured Raman spectrum of greigite in vacuum is shown in Fig. 3.6, and the calculated and experimental frequencies of the Raman active modes are shown in Table 3.1. The A_{1g} mode represents the stretching of S atoms towards the tetrahedral site Fe atom. The calculated frequency is underestimated by 10% compared to the experimental value. The E_g mode represents the bending of S – Fe_{tetra} – S bonds. The calculated frequency agrees well with the experimental value. Three T_{2g} modes that originate from the asymmetric bending of Fe – O were also observed. For the T_{2g1} and T_{2g2} modes, the calculated frequencies are underestimated by 11% and 5.5%. For the T_{2g3} mode, the calculated frequency agrees well with experiment. Interestingly, when the measurement was carried out in air, only three Raman modes with frequencies of 223 cm^{-1}, 290 cm^{-1}, and 405 cm^{-1} were found. These can be assigned to the T_{2g3}, E_g and T_{2g2} modes of Fe_3O_4, respectively.[50] Because greigite is more covalent than magnetite, the frequencies of all the greigite modes are reduced by approximately 60% with respect to magnetite. The Raman lines of greigite nearly disappeared in air, which indicates that the incident laser induced oxidation of the sample.

3.3.5 Electrical transport properties

The high purity of our sample offers the unique opportunity to investigate the electrical transport properties in Fe_3S_4. Four-probe resistance measurements were performed on pressed bar-shaped polycrystalline samples as illustrated in the inset to Fig. 3.7b. As shown in Fig. 3.7b, the linear I-V curves indicate that Ohm's law is obeyed from 20K to RT, implying good contacts between the sample and the electrodes. The temperature dependence of the resistivity was measured from 5 K to RT and is shown in Fig. 3.7b. The resistivity increases from 10.5 mΩcm at 5 K to 11.2 mΩcm at 100 K, which is characteristic behavior for a metal. The resistivity then decreases on further heating and reaches ~ 10.8 mΩcm at RT, suggesting that there is a cross-over from metallic to semiconductor-like behavior at ~100 K. This may originate from the localization of carriers or a change in hopping mechanism with varying temperature.[51] Nevertheless, the resistivity is in the poor-metal range and is 40 times smaller than the values reported by Coey et al.[31] and Paolella et al.,[51] and 7000 times smaller than the value measured on a single greigite microrod.[21] The lower resistivity can be attributed to the high purity and high crystallinity of the microcrystals. It should be noted that there is no sharp change in resistivity over the temperature range measured. The magnetization also changes continuously with temperature, as shown in Figure S6. Therefore, we can conclude that greigite exhibits no analog of the magnetite Verwey transition at ~120 K.

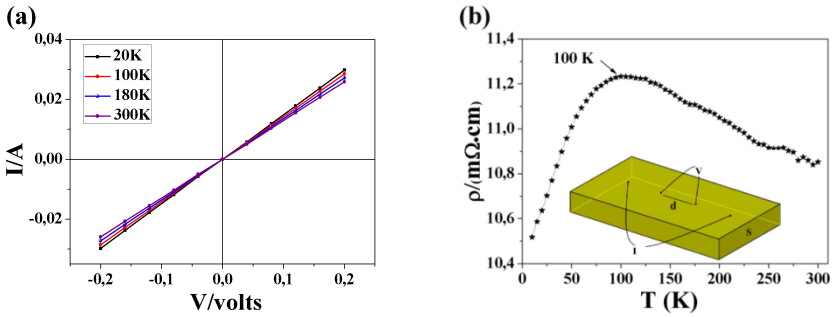

Fig. 3.7 (a) Four-probe *I-V* measurements at 20, 100, 180, and 300 K. (b) Resistivity of greigite between 5 K and 300 K and the corresponding contact geometry (inset).

It has been demonstrated that Fe_3O_4 is a half metal where the electronic density of states is 100% spin polarized at the Fermi level. This has been confirmed by both band structure calculations and experiments.[52-54] However, our recent electronic structure calculations using the previously reported room temperature crystal structure of greigite show that it is a good metal.[8] We performed analogous calculations using the 20 K structure of greigite. As seen in Figure S7, three bands intersect the Fermi energy for both the majority and minority-spin directions. The band dispersion is somewhat larger for the majority-spin direction. This band structure indicates that greigite is also a good metal at 20 K. Interestingly, we note that a study of epitaxial Fe_3O_4 (100) films grown on a W (100) single crystal indicated that the spin polarization at the Fermi level dramatically decreased in comparison with bulk samples.[55] This implies that the Fe_3O_4 (100) surface shows metallic behavior rather than the half metallic behavior exhibited by bulk samples. Considering the micron size and surfactant-coated surfaces of our greigite crystals, it is reasonable to conclude from the current evidence that our samples are representative of bulk greigite and that it shows metallic behavior, especially at lower temperatures.

3.3.6 Electrochemical properties

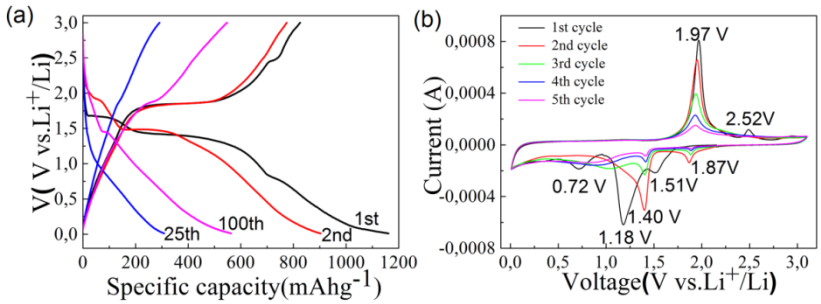

Fig. 3.8 (a) Galvanostatic charge-discharge curves of Fe_3S_4 in the voltage range 0.005-3.0 V (versus Li) at a current of 100 mAg^{-1}. (b) Cyclic voltammogram of the as-prepared Fe_3S_4 electrode at a scan rate of 0.1 $mV \bullet s^{-1}$ in the range 0.01-3.0 V (versus Li^+/Li).

Using our greigite-containing coin cells, we performed up to 100 charge-discharge cycles between 0.005-3V at a current density of 100 mA/g and at room temperature. The open-circuit voltage (OCV) of the cells is ~3.0 V and curves for selected cycles are shown in Fig.

3.8a. In the first cycle the voltage decreases sharply to 1.7 V and reaches a plateau at a capacity of ~150 mAh/g. A second voltage plateau is observed at ~1.4 V up to a capacity of ~600 mAh/g, followed by a steady decrease to the cutoff voltage of 0.01 V. This indicates that the discharge process involves a two-phase reaction.[56] For our greigite cell the first intercalation cycle gives a discharge capacity of 1161 mAh/g and a corresponding charge capacity of 1139 mAh/g. This capacity is 10 times larger than previously reported for battery anodes comprised of greigite nanoparticles.[51] The first charge profile has a long plateau at ~ 1.87 V followed by a shorter one at ~2.5 V, again consistent with a two-phase reaction. It is interesting to note that the initial discharge capacity is much higher than the theoretical value of 785 mAh/g.[57] This phenomenon has also been reported for Fe_3O_4 and Fe_2O_3 and was ascribed to the reversible formation and decomposition of a polymeric gel-like film on the particle electrode surface. This film is formed by kinetically governed electrolyte degradation driven by active metal (Fe) nanoparticles.[58, 59] In the second cycle the discharge capacity decreases to 903 mAh/g (Fig. 3.8a), while the charge capacity is 960 mAh/g. These values further decrease to 674 mAh/g and 554 mAh/g in the fifth cycle. The reduction in capacity results from large volume changes of the greigite microcrystals after lithium insertion, resulting in disintegration of the crystals and loss of the connection between the electrode materials and the current collector.[60] The capacity stops decreasing after ~20 cycles and then increases gradually to 563 mAh/g in the 100th cycle (also see Fig. S8). This is still much larger than the capacity of cells with graphite as the electrode material, 320-340 mAh/g.[59] The reason for the stability of our greigite cell is not clear. We suggest that the nanostructured Fe^0-amorphous Li_2S composite formed during the first discharge reaction needs several cycles to form a stable solid electrolyte interphase (SEI) film, allowing the greigite crystals to percolate throughout and establish intimate contact with the current collector.

In order to understand the electrochemical process, we performed cyclic voltammetry (CV) at a scanning rate of 0.1 mVs^{-1} as shown in Fig. 3.8b. In the first cycle, the reduction peak at ~1.18 V with a shoulder at ~1.51 V indicates the insertion of Li followed by the reduction of both Fe^{3+} and Fe^{2+} ions to Fe^0, forming the Fe^0-Li_2S composite as described above.[61] The reduction peak at 0.72 V is consistent with the formation of a SEI film. This is also the main reason for the irreversible capacity during the discharge process. In the subsequent oxidation scan, the material is converted to Li_2FeS_2 at ~ 1.97 V and then to FeS at ~ 2.52 V by the reaction of Li_2FeS_2 with the resulting Fe. These peaks nearly coincide with the two voltage plateaus in the galvanostatic charging curve in Figure 8A. The first and second CV profiles are different, indicating a change in mechanism in the battery. The sharp anodic peak at ~1.97 V remains whereas the peak at 2.52 V disappears. In addition, the cathodic peaks are shifted to more positive potentials from the second cycle onwards due to structural modification after the first cycle. The reduced polarization in this process indicates better reversibility. The detailed reaction in the second discharge cycle can be described as follows:

$$1.87V \quad (1)\ 2FeS + 2Li+ + 2e^- \leftrightarrow Li_2FeS_2 + Fe$$

$$1.40V \quad (2)\ Li_2FeS_2 + 2Li + 2e^- \leftrightarrow Fe + 2Li_2S$$

The cycling performance of the Fe_3S_4 electrode at a current density of 100 mA/g is displayed in Figure S8. The discharge capacity decreases continuously from 1161 mAh/g at

the first cycle to 310 mAh/g at the 25th cycle. The rate of decrease in capacity is maximum between the 1st and 2nd cycles and becomes much flatter during cycles 10-25. The initial loss of capacity may result from an incomplete conversion reaction and the irreversible loss of Li ions due to the formation of a SEI layer as discussed above. The subsequent capacity losses are perhaps caused by defects in the greigite crystals, the structure of which is shown in Fig. 3.3c. Small numbers of Li ions might be trapped in these defects, thus inducing the irreversible capacity.[62] Interestingly, the discharge capacity increases from the 25th cycle onwards and reaches 563 mAh/g after 100 cycles. This increase of capacity might be sustained over more cycles if the charge/discharge process is repeated. Similar results have been reported in many other studies, especially those with sulfides as the electrode material.[62-64] Reasons for this phenomenon are still unclear, but it might be linked to an activation process in the electrode. As the number of cycles increases, the increase in capacity is always accompanied by a decrease in the electrode impedance. The capacitance of the electrode / electrolyte interfaces was also observed to increase with cycling for some sulfides.[64] Defects and vacancies in the crystals, which trap Li ions, will tend to become more extended and facilitate the insertion of more Li ions with further cycling. In addition, the high crystallinity and low resistivity of our sample can also promote the uniform and stable delivery of electrons, further facilitating the deintercalation/intercalation of Li ions. Consequently, the transfer of electrons and Li^+ is more effective at the interface of the active materials and the electrolyte.[65]

The octahedral shape of our crystals, comprising eight (111) surfaces, might be a key factor in the high electrochemical performance. Figure 1 illustrates the atomic configurations of the (001) and (111) surfaces. The (111) plane contains a much greater density of Fe^{3+}/Fe^{2+} cations than the (001) plane. Research on the charge/discharge mechanism of spinel structures has shown that the redox reaction of M^{n+}/M^0 (where M is a transition metal) is related to the discharge capacity.[66, 67] The morphology of our greigite crystals, which is controlled by the surfactant, will thus facilitate fast $Fe^{3+}(Fe^{2+})/Fe^0$ redox reactions, resulting in excellent cycling performance as well as a high capacity.

3.4 Conclusion

We have synthesized highly pure, monodisperse greigite microcrystals using a surfactant-based hydrothermal method. We measure a saturation magnetization of 3.74 μ_B, close to the expected value of 4 μ_B (assuming a purely ionic model) and a resistivity that is 40 times lower than all previous reports on greigite, indicating the high quality of our samples. The saturation magnetization is slightly lower than 4 μ_B due to the appreciable degree of covalency involved in Fe-S bonding, as well as the possible canting of surface spins caused by the presence of surfactant molecules bonded to the surface. Greigite is different to magnetite in that it does not exhibit a Verwey transition down to 5 K, the lowest temperature investigated here. However, in contrast to previous reports, greigite is similar to magnetite in that both materials have a [111] magnetic easy axis. As an anode material for Li-ion batteries, greigite exhibits a high initial capacity of 1161 mAh/g and 562.9 mAh/g after 100 cycles. This excellent performance, combined with the fact that greigite is abundant and environmentally friendly, makes it a candidate to replace generally used graphite.

Supplementary information

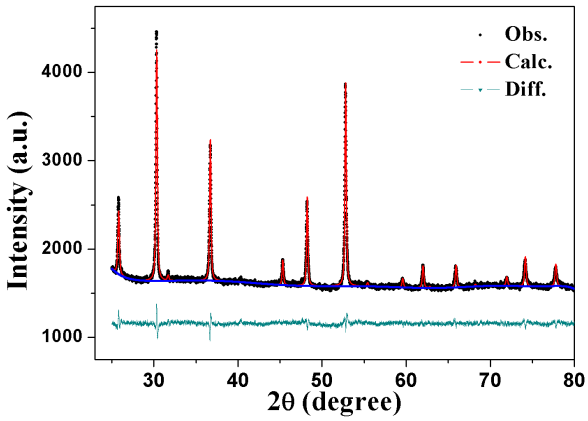

Figure S1 Observed (black data points), calculated (red line) and difference (light blue line) XRD patterns of the as-prepared sample at 20 K. Greigite at 20 K adopts space group *Fd*-3*m* with a = 9.8426(2) Å; the refined atomic coordinate of sulfur on the 32e site is $x = y = z = 0.2540(5)$.

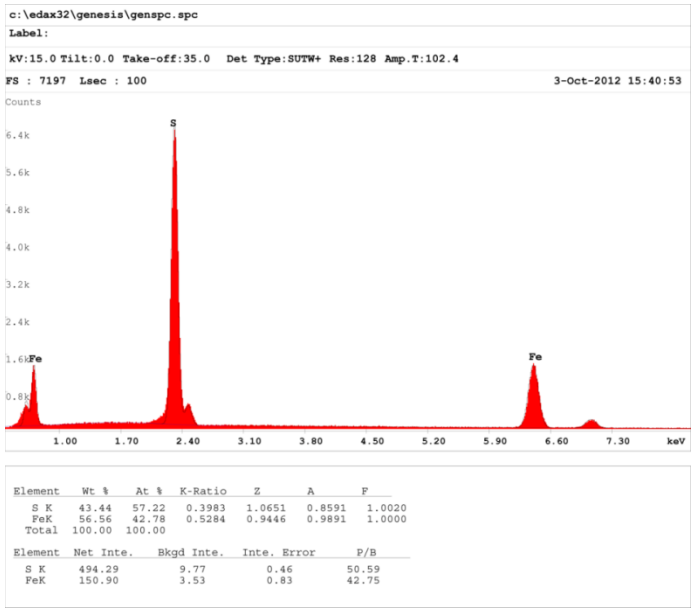

Element	Wt %	At %	K-Ratio	Z	A	F
S K	43.44	57.22	0.3983	1.0651	0.8591	1.0020
FeK	56.56	42.78	0.5284	0.9446	0.9891	1.0000
Total	100.00	100.00				

Element	Net Inte.	Bkgd Inte.	Inte. Error	P/B
S K	494.29	9.77	0.46	50.59
FeK	150.90	3.53	0.83	42.75

Figure S2 Energy Dispersive X-Ray Spectroscopy (EDS) spectrum of the as-synthesized sample

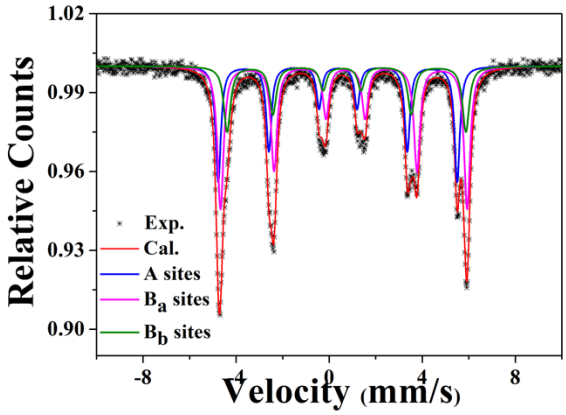

Figure S3 Fitted ^{57}Fe-Mössbauer spectrum of the Fe_3S_4 microcrystals at 80 K.

	T = 300K			80 K			300 K (with 10 kOe field)		
Parameter	*A*	B_a	B_b	*A*	B_a	B_b	*A*	B_a	B_b
δ, mm/s (+-0.01)	0.27	0.53	0.54	0.37	0.67	0.65	0.27	0.54	0.51
H, kOe (+-1)	314	314	305	319	329	319	322	305	294
S, % (+-2%)	36	46	18	32	44	24	36	47	17

Table S1 Hyperfine parameters obtained from fitting the ^{57}Fe-Mössbauer spectra at T = 300 K (zero applied field), 80 K (zero field), and 300 K (with an external magnetic field of 10 kOe): H is the magnetic hyperfine field at the ^{57}Fe nuclei, δ is the isomer shift relative to Fe, and S is the area of the spectral component.

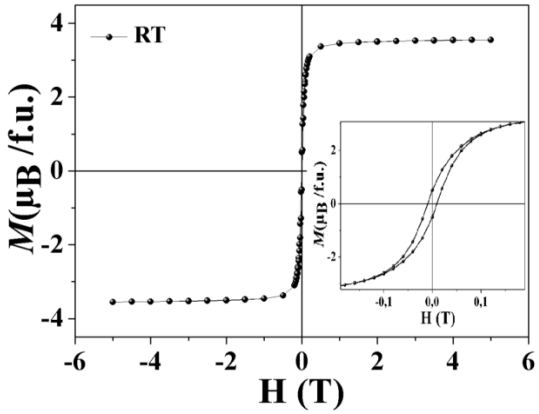

Figure S4 Magnetization versus field loops measured at 300 K. The inset shows the hysteresis in more detail.

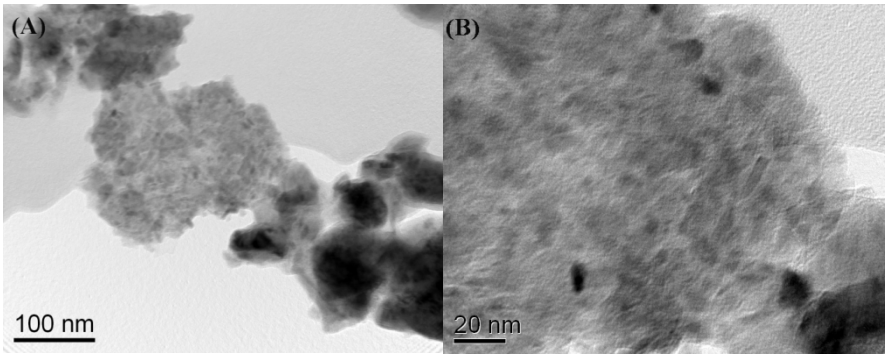

Figure S5 TEM images showing the existence of a small fraction of Fe_3S_4 nanoparticles with sizes < 10 nm

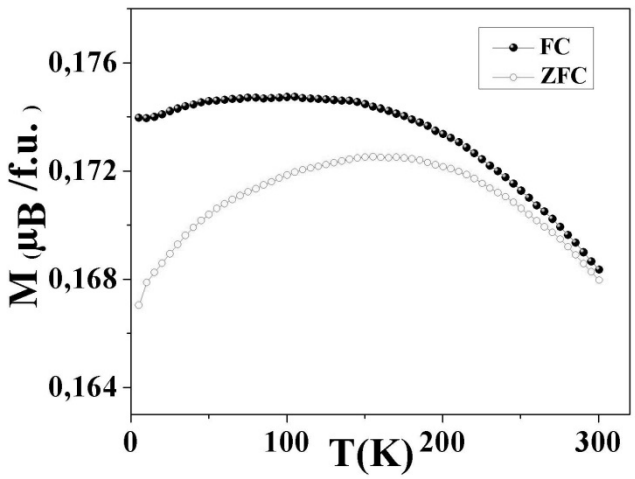

Figure S6 Zero field cooled (ZFC) and field cooled (FC) magnetization curves of greigite measured in an applied field of 100 Oe

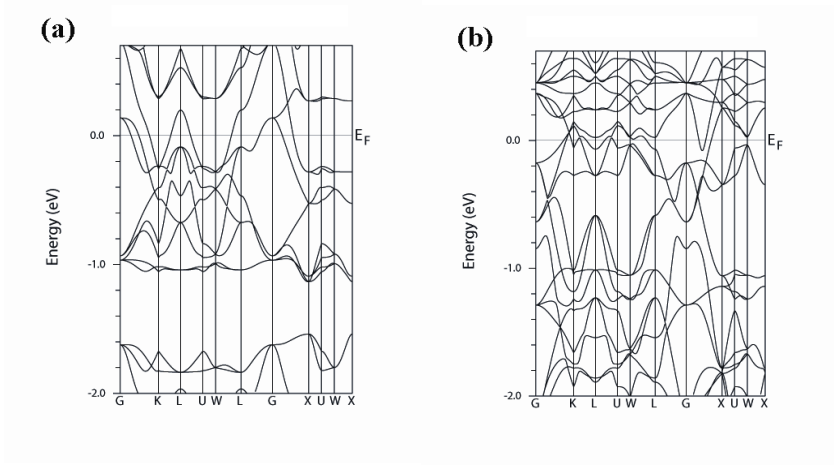

Figure S7 Calculated band structures for the majority (a) and minority (b) spin directions of greigite.

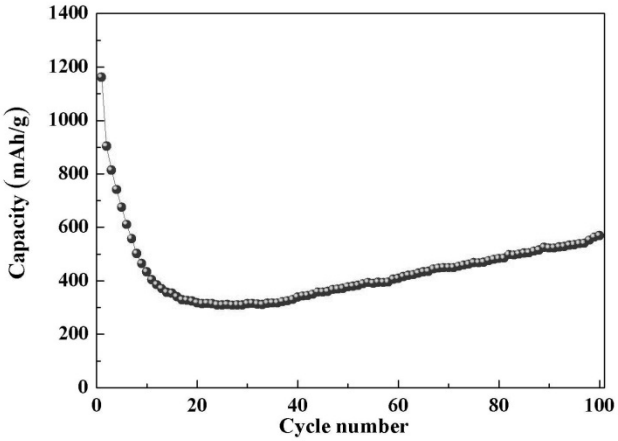

Figure S8. Cycling performance of the Fe_3S_4 electrode up to 100 cycles.

References

1. Skinner, B. J.; Erd, R. C.; Grimaldi, F. S., Greigite, The Thio-spinel of Iron; A New Mineral. *Am. Mineral.* **1964,** 49, (5-6), 543-555.
2. Roberts, A. P.; Weaver, R., Multiple Mechanisms of Remagnetization Involving Sedimentary Greigite (Fe_3S_4). *Earth Planet Sci Lett.* **2005,** 231, (3-4), 263-277.
3. Vasiliev, I.; Franke, C.; Meeldijk, J. D.; Dekkers, M. J.; Langereis, C. G.; Krijgsman, W., Putative Greigite Magnetofossils From the Pliocene Epoch. *Nat. Geosci.* **2008,** 1, (11), 782-786.
4. Snowball, I.; Thompson, R., The Occurrence of Greigite in Semidents From Loch Lomond. *J.Quaternary Sci.* **1988,** 3, (2), 121-125.
5. Rickard, D.; Luther, G. W. I., Chemistry of Iron Sulfides. *Chem. Rev.* **2007,** 107, (2), 514-562.
6. Lapen, T. J.; Righter, M.; Brandon, A. D., A Younger Age for ALH84001 and Its Geochemical Link to Shergottite Sources in Mars. *Science* **2010,** 328, (April), 347-351.
7. McKay, D. S.; Jr, G., Everett K.; Thomas-keprta, K. L.; Vali, H.; Romanek, C. S.; Clemett, S. J.; Chillier, X. D. F.; Maechling, C. R.; Zare, R. N., Search for Past Life on Mars: Possible Relic Biogenic Activity in Martian Meteorite ALH84001. *Science* **1996,** 273, (5277), 924-930.
8. Zhang, B. M.; de Wijs, G. A.; de Groot, R. A., Switchable Fermi SurfaceSheets in Greigite. *Phys. Rev. B* **2012,** 86, (020406).
9. Jia, X. L.; Chen, Z.; Cui, X.; Peng, Y. T.; Wang, X. L.; Wang, G.; Wei, F.; Lu, Y. F., Building Robust Architectures of Carbon and Metal Oxide Nanocrystals Toward High-Performance Anodes for Lithium-Ion Batteries. *ACS Nano* **2012,** 6, (11), 9911-9919.
10. Cao, F.; Hu, W.; Zhou, L.; Shi, W.; Song, S.; Lei, Y., 3D Fe_3S_4 Flower-like Microspheres: High-yield Synthesis via a Biomolecule-assisted Solution Approach, Their Electrical, Magnetic and Electrochemical Hydrogen Storage Properties. *Dalton. Trans.* **2009,** 14, (42), 9246-9252.
11. Chang, Y. S.; Savitha, S.; Sadhasivam, S.; Hsu, C. K.; Lin, F. H., Fabrication, Characterization, and Application of Greigite Nanoparticles for Cancer Hyperthermia. *J. Colloid. Interface. Sci.* **2011,** 363, (1), 314-319.
12. Feng, M.; Lu, Y.; Yang, Y.; Zhang, M.; Xu, Y. J.; Gao, H. L.; Dong, L.; Xu, W. P.; Yu, S. H., Bioinspired Greigite Magnetic Nanocrystals: Chemical Synthesis and Biomedicine Applications. *Sci. Rep.* **2013,** 3, 2994.
13. Chang, L.; Rainford, B. D.; Stewart, J. R.; Ritter, C.; Roberts, A. P.; Tang, Y.; Chen, Q., Magnetic Structure of Greigite (Fe_3S_4) Probed by Neutron Powder Diffraction and Polarized Neutron Diffraction. *J. Geophys. Res.* **2009,** 114, (B7), B07101.
14. Roberts, A. P.; Chang, L.; Rowan, C. J.; Horng, C. S.; Florindo, F., Magnetic Properties of Sedimentary Greigite (Fe_3S_4): An Update. *Rev. Geophys.* **2011,** 49, (1), RG1002.
15. Letard, I.; Sainctavit, P.; Menguy, N.; Valet, J. P.; Isambert, A.; Dekkers, M.; Gloter, A., Mineralogy of Greigite Fe_3S_4. *Phys. Scr.* **2005,** T115, 489-491.
16. Dekkers, M. J.; Passier, H. F.; Schoonen, M. A. A., Magnetic Properties of Hydrothermally Synthesized Greigite (Fe_3S_4)—High-and Low-temperature Characteristics. *Geophys. J. Inter.* **2000,** 141, (3), 809-819.
17. Akhtar, M.; Akhter, J.; Malik, M. A.; O'Brien, P.; Tuna, F.; Raftery, J.; Helliwell, M., Deposition of Iron Sulfide Nanocrystals From Single Source Precursors. *J. Mater. Chem.* **2011,** 21, (26), 9737-9745.
18. Zhang, Y.; Du, Y.; Xu, H.; Wang, Q., Diverse-shaped Iron Sulfide Nanostructures Synthesized from a Single Source Precursor Approach. *CrystEngComm* **2010,** 12, (11), 3658-3663.
19. Xing, R.; Liu, S., Facile Synthesis of Fluorescent Porous Zinc Sulfide Nanospheres and Their Application for Potential Drug Delivery and Live Cell Imaging. *Nanoscale* **2012,** 4, (10), 3135-3140.
20. Lebedev, O. I.; Turner, S.; Liu, S.; Cool, P.; Van Tendeloo, G., New Nano-architectures of Mesoporous Silica Spheres Analyzed by Advanced Electron Microscopy. *Nanoscale* **2012,** 4, (5), 1722-1727.

21. He, Z.; Yu, S. H.; Zhou, X.; Li, X.; Qu, J., Magnetic-Field-Induced Phase-Selective Synthesis of Ferrosulfide Microrods by a Hydrothermal Process: Microstructure Control and Magnetic Properties. *Adv. Funct. Mater.* **2006,** 16, (8), 1105-1111.
22. Chang, L.; Roberts, A. P.; Muxworthy, A. R., Magnetic Characteristics of Synthetic Pseudo-single-domain and Multidomain Greigite (Fe_3S_4). *Geophys. Res. Lett.* **2007,** 34, 1-6.
23. Wang, J.; Cao, S.-H.; Wu, W.; Zhao, G.-m., The Curie temperature and magnetic exchange energy in half-metallic greigite Fe3S4. *Physica Scripta* **2011,** 83, (4), 045702.
24. Devey, A.; Grau-Crespo, R.; de Leeuw, N., Electronic and magnetic structure of Fe3S4: GGA+U investigation. *Physical Review B* **2009,** 79, (19).
25. Bauer, E.; Man, K. L.; Pavlovska, A.; Locatelli, A.; Menteş, T. O.; Niño, M. A.; Altman, M. S., Fe_3S_4 (greigite) formation by vapor–solid reaction. *J. Mater. Chem. A* **2014,** 2, (6), 1903.
26. Lennie, A. R.; Redfern, S. A. T., Transformation of Mackinawite to Greigite: An in Situ X-ray Powder Diffraction and Transmission Electron Microscope study. *Am. Mineral.* **1997,** 82, 302-309.
27. Jiao, Z.; Chen, T.; Xiong, J.; Wang, T.; Lu, G.; Ye, J.; Bi, Y., Visible-light-driven photoelectrochemical and photocatalytic performances of Cr-doped $SrTiO_3/TiO_2$ heterostructured nanotube arrays. *Sci. Rep.* **2013,** 3, 2720.
28. Chang, L.; Roberts, A. P.; Tang, Y.; Rainford, B. D.; Muxworthy, A. R.; Chen, Q., Fundamental Magnetic Parameters from Pure Synthetic Greigite (Fe_3S_4). *J. Geophys. Res.* **2008,** 113, (B6), B06104.
29. Lyubutin, I. S.; Lin, C. R.; Korzhetskiy, Y. V.; Dmitrieva, T. V.; Chiang, R. K., Mössbauer spectroscopy and magnetic properties of hematite/magnetite nanocomposites. *Journal of Applied Physics* **2009,** 106, (3), 034311.
30. Lyubutin, I. S.; Starchikov, S. S.; Lin, C. R.; Lu, S. Z.; Shaikh, M. O.; Funtov, K. O.; Dmitrieva, T. V.; Ovchinnikov, S. G.; Edelman, I. S.; Ivantsov, R., Magnetic, Structural, and Electronic Properties of Iron Sulfide Fe_3S_4 Nanoparticles Synthesized by the Polyol mediated process. *J. Nanopart. Res.* **2013,** 15, (1), 1397-1409.
31. Erd, R. C.; Evans Jr, H. T., The Compound Fe_3S_4 (Smythite) Found in Nature. *J. Am. Chem. Soc.* **1956,** 78, (9), 2017.
32. Furukawa, F.; Barnes, H. L., Reactions Forming Smythite, Fe_9S_{11}. *Geochim. Cosmochim. Acta* **1996,** 60, (19), 3581-3591.
33. Van Diepen, A. M., The B-site Mössbauer Linewidth in Fe_3O_4. *Phys.Lett.* **1976,** 57A, (4), 354-356.
34. Coey, J. M. D.; Spender, M. R.; Morrish, A. H., The Magnetic Structure of the Spinel Fe_3S_4. *Solid. State. Commun.* **1970,** 8, 1605-1608.
35. De Grave, E.; Persoons, R.; Vandenberghe, R.; de Bakker, P., Mössbauer study of the high-temperature phase of Co-substituted magnetites, $CoxFe_{3-x}O_4$. I. $x \leqslant 0.04$. *Phys. Rev. B* **1993,** 47, (10), 5881-5893.
36. Chang, L.; Winklhofer, M.; Roberts, A. P.; Dekkers, M. J.; Horng, C.-S.; Hu, L.; Chen, Q., Ferromagnetic Resonance Characterization of Greigite (Fe_3S_4), Monoclinic Pyrrhotite (Fe_7S_8), and Non-interacting Titanomagnetite ($Fe_{3-x}Ti_xO_4$). *Geochem. Geophy. Geosy.* **2012,** 13, 1-19.
37. Winklhofer, M.; Chang, L.; Eder, S. H. K., On the magnetocrystalline anisotropy of greigite (Fe3S4). *Geochemistry, Geophysics, Geosystems* **2014,** 15, (4), 1558-1579.
38. Chikazumi, S., Physics of Magnetism. *New York: Wiley* **1964**, 277.
39. Chang, L.; Rainford, B. D.; Stewart, J. R.; Ritter, C.; Roberts, A. P.; Tang, Y.; Chen, Q., Magnetic structure of greigite (Fe3S4) probed by neutron powder diffraction and polarized neutron diffraction. *Journal of Geophysical Research* **2009,** 114, (B7).
40. Morr, A. H.; Haneda, K.; Morrish, A. H., Magnetic Structure of Small $NiFe_2O_4$ Particles. *J. Appl. Phys.* **1981,** 52, (3), 2496-2498.

41. Lin, D.; Nunes, A. C.; Majkrzak, C. F.; Berkowitz, A. E., Polarized Neutron Study of the Magnetization Density Distribution within a $CoFe_2O_4$ colloidal particle. *J. Magn. Magn. Mater.* **1995,** 145, 343-348.
42. Berkowitz, A.; Lahut, J.; Jacobs, I.; Levinson, L.; Forester, D., Spin Pinning at Ferrite-Organic Interfaces. *Phys. Rev. Lett.* **1975,** 34, (10), 594-597.
43. Kodama, R. H.; Berkowitz, A. E.; McNiff, E. J.; Foner, S., Surface Spin Disorder in $NiFe_2O_4$ Nanoparticles. *Phys. Rev. Lett.* **1996,** 77, 394-397.
44. Pike, C. R.; Roberts, A. P.; Verosub, K. L., Characterizing Interactions in Fne Magnetic Particle Systems Using First Order Reversal Curves. *J. Appl. Phys.* **1999,** 85, (9), 6660-6667.
45. Roberts, A. P.; Liu, Q.; Rowan, C. J.; Chang, L.; Carvallo, C.; Torrent, J.; Horng, C.-S., Characterization of Hematite (α-Fe_2O_3), Goethite (α-FeOOH), Greigite (Fe_3S_4), and Pyrrhotite (Fe_7S_8) Using First-order Reversal Curve Diagrams. *J. Geophys. Res.* **2006,** 111, (B12), B12S35.
46. Wang, N.; Cao, X.; Guo, L.; Yang, S. H.; Wu, Z. Y., Facile Synthesis of PbS Truncated Octahedron Crystals with High Symmetry and Their Large-scale Assembly into Regular Patterns by a Simple Solution Route. *ACS Nano* **2008,** 2, (2), 184-190.
47. Niu, Z.; Li, Y., Removal and Utilization of Capping Agents in Nanocatalysis. *Chem. Mater.* **2013**, DOI: 10.1021/cm4022479.
48. Rémazeilles, C.; Saheb, M.; Neff, D.; Guilminot, E.; Tran, K.; Bourdoiseau, J.-A.; Sabot, R.; Jeannin, M.; Matthiesen, H.; Dillmann, P.; Refait, P., Microbiologically Influenced Corrosion of Archaeological Artefacts: Characterisation of Iron(II) Sulfides by Raman Spectroscopy. *J. Raman Spectrosc.* **2010,** 41, (11), 1425-1433.
49. White, W. B.; Deangelis, B. A., Interpretation of the Vibrational Spectra of Spinels. *Spectrochimica Acta A* **1967,** 23A, 985-995.
50. Shebanova, O. N.; Lazor, P., Raman Spectroscopic Study of Magnetite ($FeFe_2O_4$): a New Assignment for the Vibrational Spectrum. *J. Solid State Chem.* **2003,** 174, (2), 424-430.
51. Paolella, A.; George, C.; Povia, M.; Zhang, Y.; Krahne, R.; Gich, M.; Genovese, A.; Falqui, A.; Longobardi, M.; Guardia, P.; Pellegrino, T.; Manna, L., Charge Transport and Electrochemical Properties of Colloidal Greigite (Fe_3S_4) Nanoplatelets. *Chem. Mater.* **2011,** 23, 3762-3768.
52. Chang, M. T.; Chou, L. J.; Hsieh, C. H.; Chueh, Y. L.; Wang, Z. L.; Murakami, Y.; Shindo, D., Magnetic and Electrical Characterizations of Half-Metallic Fe_3O_4 Nanowires. *Adv. Mater.* **2007,** 19, (17), 2290-2294.
53. Groot, R. A.; Mueller, F. M., New Class of Materials: Half-Metallic Ferromagnets. *Phys. Rev. Lett.* **1983,** 50, (25), 2024-2027.
54. Zhang, D.; Liu, Z.; Han, S.; Li, C.; Lei, B., Magnetite (Fe_3O_4) Core-shell Nanowires: Synthesis and Magnetoresistance. *Nano Lett.* **2004,** 4, (11), 2151-2155.
55. Fonin, M.; Pentcheva, R.; Dedkov, Y. S.; Sperlich, M.; Vyalikh, D. V.; Scheffler, M.; Rüdiger, U.; Güntherodt, G., Surface electronic structure of the Fe_3O_4 (100) : Evidence of a half-metal to metal transition. *Physical Review B* **2005,** 72, (10), 104436.
56. Sharma, N.; Guo, X.; Du, G.; Guo, Z.; Wang, J.; Wang, Z.; Peterson, V. K., Direct Evidence of Concurrent Solid-solution and Two-phase Reactions and the Nonequilibrium Structural Evolution of $LiFePO_4$. *J. Am. Chem. Soc.* **2012,** 134, (18), 7867-7873.
57. Chen, J.; Xu, L.; Li, W.; Gou, X., Alpha-Fe_2O_3 Nanotubes in Gas Sensor and Lithium Ion Battery Applications. *Adv. Mater.* **2005,** 17, (5), 582-586.
58. Xu, J. S.; Zhu, Y. J., Monodisperse Fe_3O_4 and γ-Fe_2O_3 Magnetic Mesoporous Microspheres as Anode Materials for Lithium-ion Batteries. *ACS Appl. Mater. Interfaces* **2012,** 4, (9), 4752-4757.
59. Yu, Y.; Chen, C. H.; Shui, J. L.; Xie, S., Nickel-foam-supported reticular CoO-Li_2O composite anode materials for lithium ion batteries. *Angew. Chem. Int. Ed.* **2005,** 44, (43), 7085-7089.
60. Wang, X. L.; Han, W. Q.; Chen, H.; Bai, J.; Tyson, T. A.; Yu, X. Q.; Wang, X. J.; Yang, X. Q., Amorphous Hierarchical Porous GeO(x) as High-capacity Anodes for Li ion Batteries with Very Long Cycling Life. *J. Am. Chem .Soc.* **2011,** 133, (51), 20692-20695.

61. Reddy, M. V.; Yu, T.; Sow, C. H.; Shen, Z. X.; Lim, C. T.; Subba Rao, G. V.; Chowdari, B. V. R., α-Fe_2O_3 Nanoflakes as an Anode Material for Li-Ion Batteries. *Adv. Funct. Mater.* **2007,** 17, (15), 2792-2799.
62. Chang, K.; Wang, Z.; Huang, G. H.; Li, H.; Chen, W. X.; Lee, J. Y., Few-layer SnS_2/graphene Hybrid with Exceptional Electrochemical Performance as Lithium-ion Battery Anode. *J. Power Sources* **2012,** 201, 259-266.
63. Du, Y.; Yin, Z.; Zhu, J.; Huang, X.; Wu, X. J.; Zeng, Z.; Yan, Q.; Zhang, H., A General Method for the Large-scale Synthesis of Uniform Ultrathin Metal Sulphide Nanocrystals. *Nat. Commun.* **2012,** 3, 1-7.
64. Chang, K.; Geng, D. S.; Li, X. F.; Yang, J. L.; Tang, Y. J.; Cai, M.; Li, R. Y.; Sun, X. L., Ultrathin MoS_2/Nitrogen-Doped Graphene Nanosheets with Highly Reversible Lithium Storage. *Adv. Energy Mater.* **2013,** 3, (7), 839-844.
65. Xiong, Q. Q.; Tu, J. P.; Lu, Y.; Chen, J., Hierarchical Hollow-Structured Single-Crystalline Magnetite (Fe_3O_4) Microspheres: The Highly Powerful Storage versus Lithium as an Anode for Lithium Ion Batteries. *J. Phys. Chem. C.* **2012,** 116, 6495-6502.
66. Xiao, X.; Liu, X.; Zhao, H.; Chen, D.; Liu, F.; Xiang, J.; Hu, Z.; Li, Y., Facile Shape Control of Co_3O_4 and the Effect of the Crystal Plane on Electrochemical Performance. *Adv. Mater.* **2012,** 24, (42), 5762-5766.
67. Singhana, B.; Rittikulsittichai, S.; Lee, T. R., Tridentate adsorbates with cyclohexyl headgroups assembled on gold. *Langmuir* **2013,** 29, (2), 561-9.